Journal Name

ARTICLE TYPE

Cite this: DOI: 00.0000/xxxxxxxxxx

Reversible barocaloric effects over a large temperature span in fullerite C_{60}

Junning Li,[a] David Dunstan,[a] Xiaojie Lou,[b] Antoni Planes,[c] Lluís Mañosa,[c] María Barrio,[d] Josep-Lluís Tamarit[d] and Pol Lloveras,*[d]

Received Date
Accepted Date

DOI: 00.0000/xxxxxxxxxx

Solid-state cooling methods based on field-driven first-order phase transitions are often limited by significant hysteresis and small temperature span, which increase the input work required to drive the cooling cycle reversibly and reduce the temperature range of operation. Here we show that giant reversible caloric effects can be driven using low hydrostatic pressures in the molecular crystal of fullerene C_{60} across its order-disorder first-order phase transition due to a small transition hysteresis and a high sensitivity of the transition to pressure. In particular, we obtain isothermal entropy changes $\Delta S = 25$ J K^{-1} kg^{-1} under reversible application and removal of a pressure as low as $p = 0.05$ GPa. We also demonstrate that these features allow to obtain these giant effects in a wide temperature span around room temperature which, furthermore, is desirable for single-component regenerative coolers. For a pressure change of $p = 0.41$ GPa, we obtain giant reversible values of $\Delta S = 31$ J K^{-1} kg^{-1} and $\Delta T = 11$ K, in a temperature interval larger than 50 K. This very good barocaloric performance postulates C_{60} as a one of the best candidates known so far to be considered by engineers for the development of barocaloric devices. The physics underlying these caloric effects is also analyzed.

1 Introduction

About 3400 milion of air conditioning units based on compression-expansion cycles of fluids, are installed around the world and it is expected that this number will grow four times in the next 30 years[1]. Moreover, the hidrofluorocarbon fluids used in these devices have a global warming potential up to thousands of times that of CO_2, aggravating noticeably the greenhouse effect because a significant amount of such fluids systematically leaks out to the atmosphere. Alternative cooling methods based on the solid state promise higher efficiencies and avoid the use of harmful fluids[2] and therefore this research field has received great attention in the past decades[3,4]. Fundamentally, these techniques achieve cooling from changes in temperature and entropy obtained in a controlled way via application of external stimuli. These so-called caloric effects are mostly sought at first-order phase transitions because the mentioned thermodynamic changes can be large, driving the exchange of the transition latent heat. However, first-order transitions are affected by hysteresis, which can dramatically degrade the caloric performance because, on the one hand, it increases the required input work to drive the changes cyclically forth and back with the consequent decrease in efficiency, and because, on the other hand, it reduces the temperature range of operation[5–7]. Although strategies have been proposed[8] to take advantage of hysteresis in specific cases, in general a relatively small hysteresis is required in any solid-state caloric material to be actually suitable for implementation in future devices.

Furthermore, large caloric effects driven by magnetic or electric fields are restricted to phase transitions involving changes in magnetization and polarization, respectively. In contrast, mechanically-driven large caloric effects[9] offer a much large number of candidates. In particular, any of the numerous and diverse non-isochoric transitions can be used for pressure-driven (barocaloric, BC) effects. Among them, magnetostructural alloys have traditionally received most research efforts[10–13] due to their high densities, high thermal conductivities and the possibilities of tuning the material properties via off-stoichiometry or doping[14], and by combining magnetic field and pressure for multicaloric effects[8,15–17]. Nevertheless, lately, materials undergoing transitions involving a strong order-disorder change are attracting increasing interest because the disordering process may

[a] School of Physics and Astronomy, Queen Mary University of London, London E1 4NS, United Kingdom
[b] Frontier Institute of Science and Technology and State Key Laboratory for Mechanical Behavior of Materials, Xi'an Jiaotong University, Xi'an 710049, China
[c] Departament de Física de la Matèria Condensada, Facultat de Física, Universitat de Barcelona, Martí i Franquès 1, 08028 Barcelona, Catalonia
[d] Grup de Caracterització de Materials, Departament de Física, EEBE and Barcelona Research Center in Multiscale Science and Engineering, Universitat Politècnica de Catalunya, Eduard Maristany, 10-14, 08019 Barcelona, Catalonia.* E-mail: pol.lloveras@upc.edu

† Electronic Supplementary Information (ESI) available. See DOI: 10.1039/cXsm00000x/

lead to large entropy changes and therefore may show a better BC performance. This is the case, for instance, of strong occupational disorder in some ferroelectric[18] and hybrid organic-inorganic compounds[19], and positional disorder in superionic transitions[20]. Very recently, crystals exhibiting strong orientational disorder (plastic crystals) have been identified as compounds with the largest caloric effects achieved so far in the solid state, comparable to current fluid refrigerants[21,22]. However, some are shadowed by a considerable transition hysteresis which may disqualify them for applications[5].

Carbon materials such as graphite[23], diamond[24], graphene[25,26], carbon nanotubes[27,28] and fullerenes[29] have shown superior mechanical, electrical, thermal or optical properties for practical applications. These materials have also been considered for caloric purposes, and previous theoretical studies have focused on the electrocaloric, elastocaloric and barocaloric effects of graphene[30–32], and the elastocaloric effect of carbon nanotubes[30]. However, experimental studies are still lacking in these compounds. Here we report an experimental analysis of the BC response of fullerite C_{60}, the molecular crystal of C_{60} (buckminster fullerene). We have selected this compound as a promising BC candidate because it undergoes an order-disorder transition towards a plastic crystal phase near room temperature. In this face-centered cubic (fcc) phase, the orientational disorder in C_{60} is prototypical because the quasi-spherical molecular shape permits a quasi-free rotation[33] as suggested by x-ray[34] and NMR[35] experiments and the unique excellent agreement with the Pauling-Fowler model[36]. At a temperature $T \sim 257$ K, fullerite C_{60} undergoes a first-order phase transition on cooling across which, in addition to a volume reduction, the molecular orientations order partially, reducing significantly the number of possible orientations[35,37]. As a consequence, the four sites that are equivalent in the fcc phase become distinguishable in the low-temperature phase[38], reducing the fcc symmetry to a simple cubic (sc) lattice[39,40]. This symmetry breaking can be seen in the unit cells for both sc and fcc phases shown in Fig. 1(a,b)[38,40], where the quasi-free rotating C_{60} molecules in the fcc phase are represented by spheres. Interestingly, the orientational disordering across the phase transition is a source for a giant transition entropy change ΔS_t of $\sim 25-50$ J K^{-1} kg^{-1}[33,34,41–44]. Yet giant, this value is lower than colossal values reported in other plastic crystals[45] because on the one hand the elemental rotating units are heavy rigid molecules and on the other hand in the sc phase the ordering is not complete.

The present study demonstrates that C_{60} exhibits outstanding BC properties. In particular, we show that the combination of a large transition entropy change, a small transition hysteresis and a high sensitivity of the transition to the applied pressure allows to obtain giant reversible BC effects at very small pressure changes. Moreover, at moderate pressure changes, giant reversible BC effects are obtained on a very wide temperature span, which expands the operational temperatures around room temperature and suggests its use in regenerative cooling cycles[46].

2 Experimental details

Crystalline powder of C_{60} (99.5 wt% purity) was purchased from Sigma-Aldrich and used as such. High-resolution x-ray powder diffraction (XRPD) measurements were performed at atmospheric pressure and different temperatures using an INEL diffractometer with Cu-$K_{\alpha 1} = 1.5406$ Å radiation, a curved position-sensitive detector (CPS120), a 0.5-mm-diameter Lindemann capillary and a 700 series Oxford Cryostream Cooler to control the temperature. Differential Scanning Calorimetry (DSC) at atmospheric pressure was performed using a commercial Discovery DSC 2500 (TA instruments) at 10 K min^{-1}, using 10-20 mg samples of C_{60}. Calorimetry at high pressure was performed using two Cu-Be high-pressure cells that can operate in a temperature range $\sim 200-393$ K. One (calorimeter A) is a bespoke high-pressure calorimeter that operates up to ~ 3 kbar and uses thermocouples as thermal sensors and the other (calorimeter B) is a commercial high-pressure cell MV1-30 from Unipress (Poland) adapted as a calorimeter that can operate up to ~ 6 kbar and uses Peltier modules as thermal sensors. Powdered samples of ∼200 mg of mass were mixed with an inert fluid (Galden-Bioblock Scientist) to remove air and encapsulated in tin capsules. To verify that the inert fluid was chemically inactive and did not modify thermodynamic properties of the phase transition, preliminary DSC measurements were carried out with a C60-inert fluid mixture at atmospheric pressure on the commercial Differential Scanning Calorimeter. The pressure transfer medium used was DW-Therm M90.200.02 (Huber).

3 Results and discussion

3.1 Phase transition properties at atmospheric pressure

Temperature-dependent XRPD at atmospheric pressure confirm the expected sc phase ($Pa\bar{3}$, with $Z=4$ formula units per unit cell) at low temperatures, which transforms to the fcc phase ($Fm\bar{3}m$, $Z=4$) around $T \sim 260$ K (see Fig. 1a-b and Fig. S1 and Table S1 in Supplementary Information). From the recorded XRPD patterns (see Fig. 1c-e), the temperature evolution of the unit cell volume per formula unit $V(T)/Z$ is determined by means of pattern matching (see Fig. 1f). The finite volume change at the first-order phase transition (indicated by a double arrow in the Figure) corresponds to a large relative increase on heating of $\Delta V_t/V_{sc} \sim 1\%$. Both above and well below ($T < 250$ K) the transition, $V(T)$ shows a linear behavior as indicated by the red and blue linear fits, respectively, whereas below but close to the first-order transition ($250-260$ K), $V(T)$ shows a nonlinear behavior as indicated by the second-order polynomial fit (green line). In view of previous studies[33,41–44], this nonlinear $V(T)$ regime can be associated with a pretransitional regime.

Isobaric temperature-dependent calorimetric signals render peaks in $dQ/|dT|$ (Q is heat) associated with the first-order transition (see Fig. 2a), that are positive for the sc→fcc transitions on heating (i.e. endothermic) and negative for the fcc→sc transitions on cooling (i.e. exothermic). It can be observed that exothermic peaks show a two-peak structure. This behavior has been previously reported in literature[41] and has been ascribed to the likely existence in the sc phase of two quasidegenerated orienta-

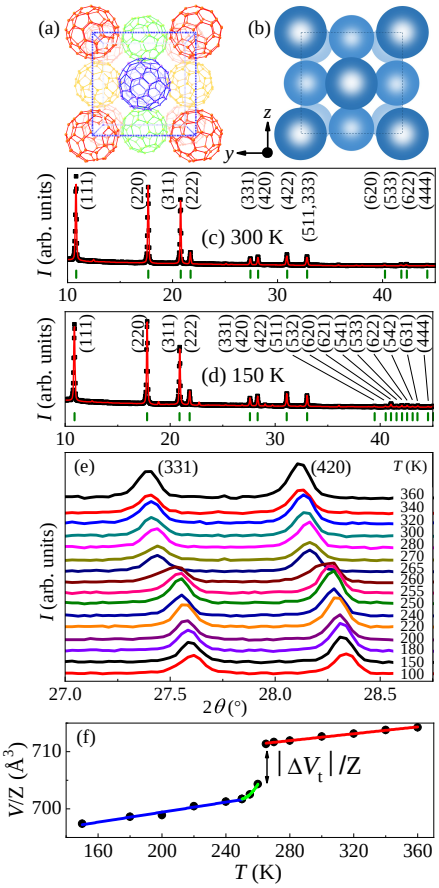

Fig. 1 (a) and (b) unit cells of the low-temperature simple cubic (sc) phase and high-temperature face-centered cubic (fcc) phase, respectively, generated from literature data[38,40]. Spheres in the fcc cell represent the C_{60} molecules under quasi-free rotation whereas C_{60} molecules with non-equivalent orientations in the sc cell[39] are plotted in different colors for clarity. (c) and (d) XRPD patterns recorded at 300 K and 150 K, corresponding to the fcc and sc phases, respectively, in the interval $2\theta = (10,45)^\circ$. Black symbols correspond to experimental data, red lines are calculated patterns via pattern matching fitting procedure and green lines indicate the position of the Bragg peaks, whose (hkl) Miller indices are indicated on top of each panel (see also Fig. S1 and table S1 in Supplementary Information for an enlargement of the diffraction peaks in the region above 40° and the (hkl) list). (e) Temperature evolution of the (331) and (420) Bragg peaks well above, across, and well below the phase transition. (f) Temperature-dependent unit cell volume on heating. Error bars are smaller than the symbol size. The finite volume change per formula unit across the phase transition, $|\Delta V_t|/Z$, is indicated by a double arrow. Red and blue lines are linear fits to $V(T)$ data above and well below the transition, respectively. Green line is a second-order polynomial fit to $V(T)$ data at the pretransitional regime. For more details see the text.

tional configurations that originate due to lattice impurities. The fact that this feature is visible only on cooling is probably due to hysteresis. Transition enthalpy changes, ΔH_t, and transition entropy changes, ΔS_t, can be obtained from integration of peaks in $dQ/|dT|$ and in $(1/T)dQ/|dT|$, respectively, after baseline subtraction between temperatures T_1 and T_2 properly chosen below and above the pressure-dependent transition range, as usual[21].

At atmospheric pressure (black curves in Fig. 2a), the peak temperatures occur at $T = 259$ K and $T = 256$ K for the transitions on heating and on cooling, respectively, exhibiting a small hysteresis of 3 K. The integrated values are $\Delta H_t(p_{atm}) = 6.9 \pm 0.5$ J g^{-1} and $\Delta S_t(p_{atm}) = 26 \pm 2$ J K^{-1} kg^{-1} on heating and $|\Delta H_t(p_{atm})| = 7.6 \pm 0.5$ J g^{-1} and $|\Delta S_t(p_{atm})| = 27 \pm 2$ J K^{-1} kg^{-1} on cooling. These values are in overall agreement with previous values reported in literature on powdered samples[34,41–43] whereas single crystals usually render larger results[33,44], which are ascribed to the purity and crystallinity of the samples. On the other hand, in this compound the baseline chosen for integration in the low-temperature interval may be a source of significant uncertainty due to a smooth tail below the transition peak corresponding to the pretransitional regime. In some cases this tail is observed to extend more than 100 K below the first-order peak[33], and may depend on the temperature rate of measurement. As our high-pressure calorimetry does not capture such pretransitional tail we can associate the integrated values entirely with the first-order transition.

For C_{60}, the entropy change across the first-order phase transition ΔS_t originates from the volume change ΔS_V and from the partial ordering of the orientation of C_{60} molecules, ΔS_c, such that $\Delta S_t = \Delta S_V + \Delta S_c$. As for ΔS_V, it can be calculated taking into account that the entropy S is related to the Helmholtz free energy F via the thermodynamic relation $S = -\left(\frac{\partial F}{\partial T}\right)_V$. Considering the high-temperature phase as the unstrained phase, the volume-related entropy change $\Delta S_V = S_V(\text{fcc}) - S_V(\text{sc}) = -S_V(\text{sc}) = \left(\frac{\partial F_V(\text{sc})}{\partial T}\right)_V$. For a cubic system experiencing a pure dilatation, F_V can be expressed up to the harmonic approximation as $F_V = \frac{K}{3\rho}\left(\varepsilon_{xx}+\varepsilon_{yy}+\varepsilon_{zz}\right)^2 = \frac{K}{3\rho}\left(\frac{\Delta V_t}{V}\right)^2$ where ε_{ii} are the diagonal terms of the lagrangian strain tensor, $K = \frac{C_{11}+2C_{12}}{3}$ is the bulk modulus, with C_{ij} the components of the stiffness tensor, $\frac{\Delta V_t}{V}$ is the relative volume change at the transition and ρ is the density. Therefore, ΔS_V can be expressed as $\Delta S_V = -\left(\frac{\partial F_V(\text{sc})}{\partial T}\right)_V = -\frac{1}{3\rho}\left(\frac{\Delta V_t}{V}\right)^2\left(\frac{\partial K}{\partial T}\right)_V$. Using $\left(\frac{\partial K}{\partial T}\right)_V = -0.04 \pm 0.02$ GPa K^{-1} from temperature-dependent elastic constants available in literature[47] and $\rho = 1.70 \cdot 10^3$ kg m^{-3}, we obtain $\Delta S_V = 1.0 \pm 0.5$ J K^{-1} kg^{-1}, which is much smaller than the total transition entropy change. Interestingly, this indicates that the major contribution to the total transition entropy change comes from the partial ordering of molecular orientation, $\Delta S_c \sim 26$ J K^{-1} kg^{-1}. Then, we can estimate the ratio between the number of configurations achievable in the fcc phase (N_1) and in the sc phase (N_2) as $N_1/N_2 = exp(MR^{-1}\Delta S_c) \sim 9.5$.

3.2 Phase transition properties at high pressures

On increasing pressure, the isobaric calorimetric peaks shift to high temperatures (see Fig. 2a), which is qualitatively consistent with the positive ΔV_t on heating as established by the Clausius-Clapeyron (CC) equation $dT/dp = \Delta V_t/\Delta S_t$ (notice that here ΔS_t is the total transition entropy change[48]). The dependence of the peak temperatures with pressure is plotted in Fig. 2b, and shows constant $dT/dp = 167 \pm 3$ K GPa^{-1} on heating and $dT/dp = 172 \pm 2$ K GPa^{-1} on cooling within the pressure range under study, which are in agreement with literature values[41,49]. The

large values for dT/dp in C_{60} anticipate a giant temperature span and along with the small difference between the endothermic and exothermic peak temperatures promise an outstanding reversibility for the BC effects, as it will be discussed in Sec. 3.4. It is worth mentioning that the use of He as pressure-transmitting medium in some studies[41,44,50] gave rise to a much smaller dT/dp, which was associated with the easy penetration of He into the lattice.

From integration of peaks in $(1/T)|dQ/dT|$ at different pressures after baseline subtraction, we obtain that the transition entropy change (see Fig. 2c) decreases with pressure notably within the pressure range under study, as $d|\Delta S_t|/dp = -30 \pm 1$ J K^{-1} kg^{-1} GPa^{-1}, averaging over heating and cooling ramps. By including this value in the CC equation and taking into account that dT/dp does not depend on pressure, it can be derived that the first-order transition volume change also decreases with pressure as $d|\Delta V_t|/dp = (dT/dp)(d\Delta S_t/dp) = (-5.3 \pm 1.0) \cdot 10^{-6}$ m^3 kg^{-1} GPa^{-1}. These results could be interpreted as a weakening of the first-order character of the transition when the pressure increases.

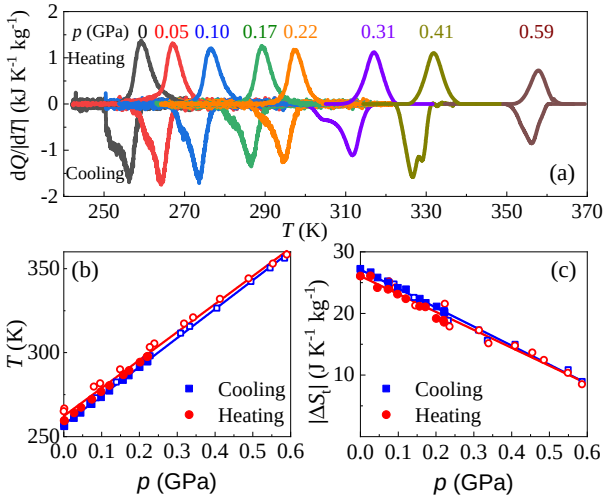

Fig. 2 (a) Temperature-dependent isobaric heat flow $dQ/|dT|$ at different pressures, after baseline subtraction. Selected curves shown below and above 0.3 GPa have been performed using calorimeter A and B, respectively. (b) Peak temperature and (c) entropy change across the phase transition ΔS_t as a function of pressure determined from both heating and cooling heat flow curves shown in panel (a). Solid and empty symbols stand for values obtained using calorimeters A and B respectively. Lines are linear fits to data.

It is worth mentioning here that we can safely state that C_{60} does not undergo polymerization nor amorphization processes because of two reasons: (i) In the present study, pressure and temperature ranges are much below the pressure and temperature above which such irreversible processes have been observed[51,52]; (ii) Pressure values for our measurements have not been chosen monotonically increasing but nearly random just to ensure that the observed transitions at different pressures are thermodynamically reversible and do not depend on history.

3.3 Determination of entropy as a function of temperature and pressure

For the calculation of the BC effects, the quasi-direct method[4] requires the knowledge of isobaric entropy vs. temperature curves at different pressures, $S(T,p)$, across and on each side of the transition. For this purpose we proceed as described in Refs[9,53]:

$$S(T,p) = \begin{cases} S(T_0,p) + \int_{T_0}^{T} \frac{C_p^{sc}(T',p)}{T'} dT', & T_0 \le T \le T_1(p) \\ S(T_1,p) + \\ \int_{T_1}^{T} \frac{1}{T'} \left(C_p^{sc\text{-}fcc}(T',p) + \frac{dQ(T',p)}{dT'} \right) dT', & T_1(p) \le T \le T_2(p). \\ S(T_2,p) + \int_{T_2}^{T} \frac{C_p^{fcc}(T',p)}{T'} dT', & T \ge T_2(p) \end{cases} \quad (1)$$

where $S(T_0,p)$ is a pressure-dependent entropy at a reference temperature T_0 chosen below the transition temperature at atmospheric pressure (in particular, we set T_0 to 150 K); $T_1(p)$ and $T_2(p)$ are pressure-dependent temperatures limiting the transition; $dQ(T,p)/dT$ is the pressure-dependent heat flow in temperature associated with the latent heat of the transition, and measured by our pressure-dependent calorimetry; $C_p^{sc}(T,p)$, $C_p^{fcc}(T,p)$ are the heat capacity of sc and fcc phases, respectively, and $C_p^{sc\text{-}fcc}(T,p) = [1-x(T,p)]C_p^{sc}(T,p) + x(T,p)C_p^{fcc}(T,p)$, where $x(T,p)$ is the fraction of the system in the high-temperature phase and is calculated as

$$x(T,p) = \frac{\int_{T_1}^{T} \frac{1}{T'} \frac{dQ(T',p)}{dT'} dT'}{\int_{T_1}^{T_2} \frac{1}{T'} \frac{dQ(T',p)}{dT'} dT'}, \qquad T_1(p) \le T \le T_2(p) \quad (2)$$

To calculate $C_p(T,p)$ throughout all the pressure-dependent temperature intervals defined in eq. 1, we have used temperature-dependent data at atmospheric pressure taken from literature[54] and have taken into account that the pressure-dependence of C_p is given by the following thermodynamic relation:

$$\left(\frac{\partial C_p}{\partial p} \right)_T = -T \left(\frac{\partial^2 V}{\partial T^2} \right)_p . \quad (3)$$

To evaluate the right-hand side of eq. 3 we have used temperature-dependent volume data shown in Fig. 1f, assuming that at any pressure[55]

$$\left(\frac{\partial V}{\partial T} \right)_p \simeq \left(\frac{\partial V}{\partial T} \right)_{p_{atm}} . \quad (4)$$

On the one hand, blue and red linear fits in Fig. 1f indicate that the temperature dependence of the unit cell volume of the sc phase below the pretransitional regime (150-250 K at atmospheric pressure) and of the fcc phase (260-360 K at atmospheric pressure) is linear. This behavior renders $\left(\frac{\partial^2 V}{\partial T^2} \right)_p \simeq 0$, which leads to a pressure independent C_p (eq. 3) in these temperature intervals (as it will be explained later on in this Section, C_p must vary with pressure in some temperature range below 150 K, where, consequently, V must be nonlinear with T).

On the other hand, below but close to the transition, C_p^{sc} literature data[54] exhibits a smooth tail corresponding to the afore-

mentioned pretransitional regime associated with the nonlinearity observed in $V(T)$ data in the temperature interval $\sim 250-260$ K (see Sec. 3.1). This behavior was fitted by a concave second-order polynomial fit (see green line in Fig. 1f), which leads to state that in this regime $\left(\frac{\partial^2 V}{\partial T^2}\right)_{p_{\rm atm}} \simeq \text{const} > 0$. Consequently, eq. 3 establishes that in this interval $\left(\frac{\partial C_p^{\rm sc}}{\partial p}\right)_T \propto -T$, i.e. $C_p^{\rm sc}$ decreases with pressure, and this decrease is larger at higher temperatures.

To account for the translation of these features to higher temperatures at higher pressures (as the transition temperature does), both extrapolation of $C_p^{\rm sc}$ and $C_p^{\rm fcc}$ in the pressure-independent regime using a Debye function fit, and shift of the pressure-dependent smooth tail in $C_p^{\rm sc}$, are carried out up to a temperature incremented by an addend $\frac{dT}{dp}(p-p_{\rm atm})$ with respect to the temperature at atmospheric pressure. Examples of temperature-dependent C_p at different pressures, i.e. $C_p(T,p)$, are shown in Fig. 3a, where the pressure-dependent and pressure-independent intervals can be distinguished. A more detailed explanation about the construction of the pressure-dependent C_p can be found in the Supplementary Information.

Lastly, the fact that, at T_0, $\left(\frac{\partial V}{\partial T}\right)_{p_{\rm atm}} \neq 0$ entails that the reference entropy must depend on pressure due to the Maxwell relation $S(T_0,p) = S(T_0,p_{\rm atm}) - \int_{p_{\rm atm}}^{p}\left(\frac{\partial V}{\partial T}\right)_{p'} dp'$, where $S(T_0,p_{\rm atm}) = \int_0^{T_0}\frac{C_p(p_{\rm atm})}{T}dT$. Assuming the condition in Eq. 4, we can write $\Delta S_+(T_0,p_{\rm atm}\rightarrow p) \equiv S(T_0,p) - S(T_0,p_{\rm atm}) \simeq \left(\frac{\partial V}{\partial T}\right)_{p_{\rm atm}}(p-p_{\rm atm})$, where $\left(\frac{\partial V}{\partial T}\right)_{p_{\rm atm}} = 3.7\cdot 10^{-8}$ m^3 kg^{-1} K^{-1} as obtained by using data in Fig. 1a. This can be understood as a signature that at temperatures well below the pressure-independent-$C_p^{\rm sc}$ regime, C_p must depend on pressure, because $S(T_0,p)$ could also be calculated directly as $S(T_0,p) = \int_0^{T_0}\frac{C_p(p)}{T}dT$ if C_p was available at pressure p.

Combining all these ingredients in eq. 1, we can finally construct the temperature-dependent isobaric entropy curves at different pressures, which are plotted in Fig. 3b and c for heating $[S_{\rm heat}(T,p)]$ and cooling $[S_{\rm cool}(T,p)]$ ramps, respectively, with respect to the reference entropy $S(T_0,p_{\rm atm})$. Notice that the procedure for constructing the entropy curves determines additional entropy changes above the transition, ΔS_+, and that at the same time this ΔS_+ can be calculated via the Maxwell relation using $\left(\frac{\partial V_{\rm fcc}}{\partial T}\right)_p$ above the phase transition. The magnitudes for this quantity obtained by using these two methods independently are in agreement within error, which confirms the validity of the constructed entropy curves.

3.4 Barocaloric effects

We now proceed to calculate the BC effects from the entropy-temperature curves determined in Sec. 3.3. Isothermal entropy changes are computed by subtracting $S(T,p)$ curves at different pressures following isothermal paths: $\Delta S(T,p_{\rm i}\rightarrow p_{\rm f}) = S(T,p_{\rm f}) - S(T,p_{\rm i})$. Hereafter, the lower pressure is taken as atmospheric pressure and the higher pressure as p, and therefore $|\Delta p| = |p_{\rm f}-p_{\rm i}| \simeq |p|$. In turn, adiabatic temperature changes are computed by subtracting the entropy-temperature curves following adiabatic paths: $\Delta T(T_{\rm s},p_{\rm i}\rightarrow p_{\rm f}) = T(S,p_{\rm f}) - T(S,p_{\rm i})$, where ΔT is more appropriately plotted as a function of the starting temperature $T_{\rm s}$. Since for a material with $dT/dp > 0$ decompressions are endothermic processes and compressions are exothermic processes, changes on first decompression are computed from entropy curves on heating whereas changes on first compression are computed from entropy curves on cooling. The corresponding results for ΔS and ΔT are shown in Fig. 4a and b, respectively. It is worth pointing out here that from the entropy curves we can state that at low pressures the main contribution to ΔS originates from the transition entropy change $\Delta S_{\rm t}$. At high pressures $\Delta S_{\rm t}$ decreases noticeably but additional entropy changes outside the transition ΔS_+ become very significant, reaching about $\sim 50\%$ of ΔS under a pressure change of $p = 0.59$ GPa.

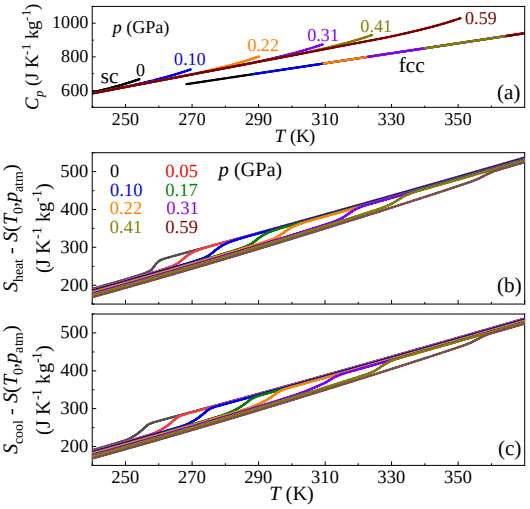

Fig. 3 (a) Pressure-dependent heat capacity constructed from literature data[54] at atmospheric pressure. For more details see the text. (b,c) Temperature-dependent isobaric entropy curves at different pressures on (b) heating and (c) cooling.

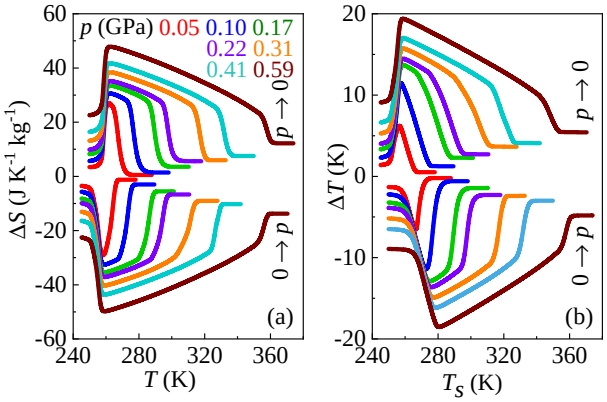

Fig. 4 Barocaloric effects obtained on first application or removal of pressure. (a) Isothermal entropy changes on decompression and compression as a function of temperature at different pressures. (b) Adiabatic temperature changes on decompression and compression as a function of the starting temperature at different pressures.

As barocaloric cooling devices work in compression - decompression cycles, it is necessary for applications to determine the

BC effects that occur when applying and removing pressure repeatedly. Given that compression processes end at cooling entropy curves at high pressure [$S_{cool}(T,p)$] whereas decompression processes end at heating entropy curves at atmospheric pressure [$S_{heat}(T,p_{atm})$], reversible BC effects are given by the difference between entropy curves on cooling at high pressure and the entropy curve on heating at atmospheric pressure. Therefore, reversible ΔT is calculated as $|\Delta T_{rev}(p_{atm} \leftrightarrow p)| = |T(S_{cool},p) - T(S_{heat},p_{atm})|$. Obviously, this expression is only valid provided that the shift of the transition by application of pressure overcomes the transition hysteresis, which establishes a lower threshold for the pressure change to obtain nonzero $|\Delta T_{rev}|$, i.e. $p \geq p_{rev}^{\Delta T}$. Nonetheless, it has been shown[6,56] that a fraction of ΔS can be achieved reversibly (ΔS_{rev}) at $p_{rev}^{\Delta S} < p_{rev}^{\Delta T}$ due to the existence of minor loops allowed by partial transformation of the sample. Above this threshold pressure change, $\Delta S_{rev}(T, p_{atm} \leftrightarrow p)$ is determined as the overlap between $\Delta S(T)$ on compression and $\Delta S(T)$ on decompression. Using the procedure described elsewhere[5] we obtain that for fullerite C_{60} across its sc→fcc transition, $p_{rev}^{\Delta S} = 0$ and $p_{rev}^{\Delta T} = 0.02 \pm 0.01$ GPa.

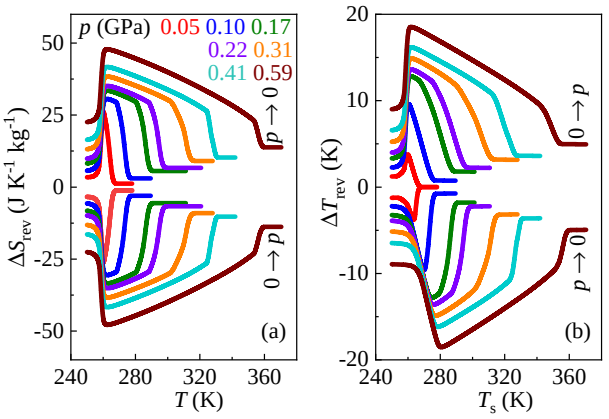

Fig. 5 Reversible barocaloric effects. (a) Reversible isothermal entropy changes on decompression and compression as a function of temperature at different pressures. (b) Reversible adiabatic temperature changes on decompression and compression as a function of the starting temperature at different pressures.

From Figs. 4 and 5, the maximum of $|\Delta S|$, $|\Delta T|$, $|\Delta S_{rev}|$ and $|\Delta T_{rev}|$ as a function of pressure change are determined and shown in Fig. 6a,b. Very interestingly, it can be observed that $|\Delta S_{rev}| > 0$ is obtained at any pressure change, as anticipated previously, and reaches $|\Delta S_{rev}| = 25 \pm 3$ J K^{-1} kg^{-1} for $p = 0.05$ GPa and $|\Delta S_{rev}| = 32 \pm 3$ J K^{-1} kg^{-1} for $p = 0.1$ GPa. Larger values can be obtained at higher pressures. The area below the $|\Delta S_{rev}|$ vs. T curves gives an estimation of the Refrigerant Capacity (RC), which refers to the amount of heat that can be exchanged cyclically between hot and cold ends[57]. Values for RC as a function of the pressure change are shown in Fig. 6c.

Importantly, giant and reversible BC effects in C_{60} are obtained in a large temperature interval. In particular, Figure 7 shows the temperature span as a function of the pressure range where an interval of ΔS_{rev} [panel (a)] and ΔT_{rev} [panel (b)] values can be achieved. At a given pressure change, the upper bound for T_{span}

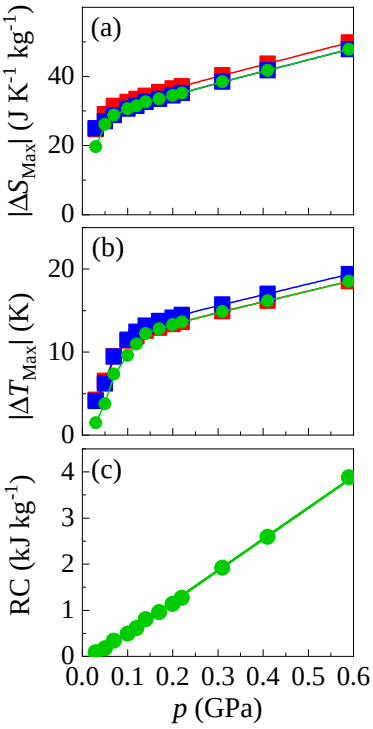

Fig. 6 Maximum (a) isothermal entropy changes and (b) adiabatic temperature changes as a function of pressure change, on first decompression (red), on first compression (blue) and reversible values (green). (c) Refrigerant capacity as a function of pressure

limiting each color band corresponds to the minimum values of the BC effects indicated in the legend so that larger BC effects are obtained in a narrower T_{span} as expected. As examples, under a pressure change of $p = 0.1$ GPa, we obtain $\Delta S_{rev} = 25 \pm 3$ J K^{-1} kg^{-1} and $\Delta T_{rev} = 5.0 \pm 0.5$ K in a temperature interval of 11 K, and under a pressure change of $p = 0.41$ GPa, we obtain $\Delta S_{rev} = 31 \pm 3$ J K^{-1} kg^{-1} and $\Delta T_{rev} = 11 \pm 1$ K in a temperature interval of about 50 K. This excellent performance can be very useful in single-compound regenerative cooling methods, where heat sources and sinks are separated by large temperature spans by means of a regenerative heat exchanger[46].

Finally, we carry out a comparison of the BC performance between different compounds by computing the Coefficient of Refrigeration Performance (CRP)[58,59], as shown in Table 1. Interestingly, it reveals that the CRP for C_{60} surpasses other compounds at room temperature and compares well with most of the remaining compounds at any temperature.

4 Summary and conclusions

We have used isobaric calorimetry at high-pressure and x-ray diffraction to complete the information needed to predict the barocaloric performance of crystalline powder of C_{60}. Our results show giant isothermal entropy changes at low pressures, that arise mainly due to the partial ordering of molecular orientations across the first-order phase transition fcc → sc. With increasing pressure the transition entropy change decreases but the isothermal entropy change still increases due to the increase in additional changes arising outside the transition

Table 1 Coefficient of Refrigeration Performance and associated quantities in giant barocaloric materials.

Material	T_t K	ΔT_{rev} K	ΔS J K^{-1} kg^{-1}	p GPa	ΔV 10^{-6} m^3 kg^{-1}	CRP	Ref.
$Fe_{49}Rh_{51}$	310	5	12.5	0.25	1.0	0.50	13,57
$MnCoGeB_{0.03}$	286	10	30	0.17	5.0	0.71	11
$Ni_{50}Mn_{31.5}Ti_{18.5}$	243	7.3	74	0.40	2.8	0.96	5
$BaTiO_3$	400	4	1.6	0.10	0.19	0.67	53
$(NH_4)_2SO_4$	219	8	60	0.10	2.9	3.31	18
AgI	390	18	60	0.25	7.4	1.17	20
[TPrA]Mn[dca]$_3$	330	4.1	30	0.007	10.0	3.51	19
[TPrA]Cd[dca]$_3$	385	1.4	11.5	0.007	5.3	0.87	19
$MnNiSi_{0.61}FeCoGe_{0.39}$	311	6	52	0.26	3.6	0.67	12
$(CH_3)_2C(CH_2OH)_2$	315	6	450	0.20	46	0.59	21
$(CH_3)C(CH_2OH)_3$	354	10	490	0.24	38	1.07	5,45
$(CH_3)_3C(CH_2OH)$	235.7	16	320	0.26	45.5	0.87	5,45
C_{60}	257	9.7	32	0.10	4.6	1.35	this work
C_{60}	257	16	42	0.41	4.6	0.71	this work

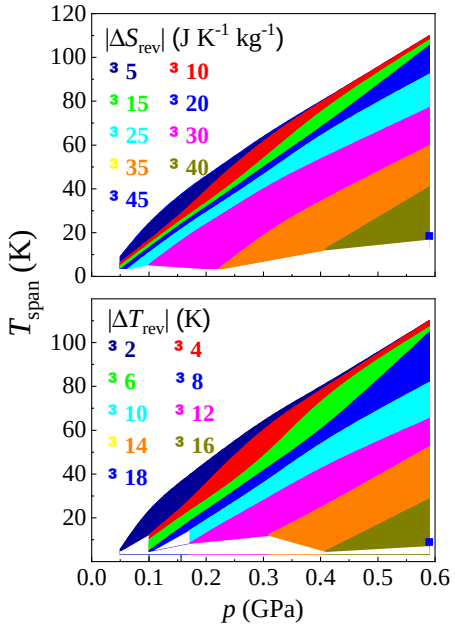

Fig. 7 Temperature span as a function of applied pressure change for which different intervals of (a) reversible isothermal entropy changes and (b) reversible adiabatic temperature changes are obtained. For more details see the text.

associated with the thermal expansion of each phase. Giant adiabatic temperature changes are also obtained, originating in a large sensitivity of the transition to pressure due to a very large transition volume change, relative to the magnitude of the transition entropy change. More importantly for applications, we demonstrate that the small hysteresis in this compound yields giant barocaloric effects that can be driven reversibly with very low pressures. In addition, the giant BC effects in C_{60} are obtained in a very large temperature span, which can be very useful in single-component cooling methods using regeneration. Our outcomes indicate that C_{60} can be a promising candidate to be employed in future barocaloric cooling devices.

Conflicts of interest

The use of the compound studied in this work for barocaloric cooling is covered in the following patent: X. Moya, A. Avramenko, L. Mañosa, J.-Ll. Tamarit and P. Lloveras, Use of barocaloric materials and barocaloric devices, PCT/EP2017/076203 (2017). The remaining authors declare no conflicts of interests.

Acknowledgements

This work was supported by the MINECO projects MAT2016-75823-R and FIS2017-82625-P, the DGU project 2017SGR-42. J. Li would like to thank China Scholarship Council (CSC) and Queen Mary joint scholarship for his stay in U.K. J. Li would like to thank Y. Tao for her support. We thank Dr. M. Baxendale for C_{60} samples, and D. J. Dennis, A. Phillips, and B. Dkhil for discussion.

Notes and references

1 `https://www.birmingham.ac.uk/Documents/college-eps/energy/Publications/2018-clean-cold-report.pdf`, (accessed November 2019).

2 *Energy Savings Potential and RD&D Opportunities for Non-Vapor-Compression HVAC Technologies*, `https://www.energy.gov/sites/prod/files/2014/03/f12/NonVapor%20Compression%20HVAC%20Report.pdf`, (accessed July 2019).

3 L. Mañosa, A. Planes and M. Acet, *J. Mater. Chem. A*, 2013, **1**, 4925–4936.

4 X. Moya, S. Kar-Narayan and N. D. Mathur, *Nat. Mater*, 2014, **13**, 439.

5 A. Aznar, P. Lloveras, M. Barrio, P. Negrier, A. Planes, L. Mañosa, N. D. Mathur, X. Moya and J.-L. Tamarit, *J. Mater. Chem. A*, 2020, **8**, 639–647.

6 B. Emre, S. Yüce, E. Stern-Taulats, A. Planes, S. Fabbrici, F. Albertini and L. Mañosa, *J. Appl. Phys.*, 2013, **113**, 213905.

7 T. Hess, L. M. Maier, N. Bachmann, P. Corhan, O. Schäfer-Welsen, J. Wöllenstein and K. Bartholomé, *J. Appl. Phys.*, 2020, **127**, 075103.

8 T. Gottschall, A. Gràcia-Condal, M. Fries, A. Taubel, L. Pfeuffer, L. Mañosa, A. Planes, K. P. Skokov and O. Gutfleisch, *Nat. Mater.*, 2018, **17**, 929–934.

9 L. Mañosa and A. Planes, *Adv. Mater.*, 2017, **29**, 1603607.

10 L. Mañosa, D. González-Alonso, A. Planes, E. Bonnot, M. Barrio, J. L. Tamarit, S. Aksoy and M. Acet, *Nat. Mater.*, 2010, **9**, 478–481.

11 A. Aznar, P. Lloveras, J.-Y. Kim, E. Stern-Taulats, M. Barrio, J. L. Tamarit, C. F. Sánchez-Valdés, J. L. Sánchez Llamazares, N. D. Mathur and X. Moya, *Adv. Mater.*, 2019, **31**, 1903577.

12 P. Lloveras, T. Samanta, M. Barrio, I. Dubenko, N. Ali, J.-L. Tamarit and S. Stadler, *APL Mater.*, 2019, **7**, 061106.

13 E. Stern-Taulats, A. Gràcia-Condal, A. Planes, P. Lloveras, M. Barrio, J.-L. Tamarit, S. Pramanick, S. Majumdar and L. Mañosa, *Appl. Phys. Lett.*, 2015, **107**, 152409.

14 E. Stern-Taulats, A. Planes, P. Lloveras, M. Barrio, J.-L. Tamarit, S. Pramanick, S. Majumdar, S. Yüce, B. Emre, C. Frontera and L. Mañosa, *Acta Mater.*, 2015, **96**, 324 – 332.

15 E. Stern-Taulats, T. Castán, L. Mañosa, A. Planes, N. D. Mathur and X. Moya, *MRS Bulletin*, 2018, **43**, 295–299.

16 L. Caron, N. T. Trung and E. Brück, *Phys. Rev. B*, 2011, **84**, 020414(R).

17 J. Liu, T. Gottschall, K. P. Skokov, J. D. Moore and O. Gutfleisch, *Nat. Mater.*, 2012, **11**, 620–626.

18 P. Lloveras, E. Stern-Taulats, M. Barrio, J. Tamarit, S. Crossley, W. Li, V. Pomjakushin, A. Planes, L. Mañosa, N. D. Mathur and X. Moya, *Nat. Commun.*, 2015, **6**, 8801.

19 J. M. Bermúdez-García, M. Sánchez-Andújar, S. Castro-García, J. López-Beceiro, R. Artiaga and M. A. Senarís-Rodríguez, *Nat. Commun.*, 2017, **8**, 15715.

20 A. Aznar, P. Lloveras, M. Romanini, M. Barrio, J.-L. Tamarit, C. Cazorla, D. Errandonea, N. D. Mathur, A. Planes, X. Moya and L. Mañosa, *Nat. Commun.*, 2017, **8**, 1851.

21 P. Lloveras, A. Aznar, M. Barrio, P. Negrier, C. Popescu, A. Planes, L. Mañosa, E. Stern-Taulats, A. Avramenko, N. D. Mathur, X. Moya and J.-L. Tamarit, *Nat. Commun.*, 2019, **10**, 1803.

22 B. Li, Y. Kawakita, S. Ohira-Kawamura, T. Sugahara, H. Wang, J. Wang, Y. Chen, S. I. Kawaguchi, S. Kawaguchi, K. Ohara, K. Li, D. Yu, R. Mole, T. Hattori, T. Kikuchi, S.-I. Yano, Z. Zhang, Z. Zhang, W. Ren, S. Lin, O. Sakata, K. Nakajima and Z. Zhang, *Nature*, 2019, **567**, 506–510.

23 R. Sengupta, M. Bhattacharya, S. Bandyopadhyay and A. K. Bhowmick, *Prog. Polym. Sci.*, 2011, **36**, 638 – 670.

24 E. A. Ekimov, V. A. Sidorov, E. D. Bauer, N. N. Mel'nik, N. J. Curro, J. D. Thompson and S. M. Stishov, *Nature*, 2004, **428**, 542 – 545.

25 M. J. Allen, V. C. Tung and R. B. Kaner, *Chem. Rev.*, 2010, **110**, 132–145.

26 A. K. Geim and K. S. Novoselov, *Nat. Mater.*, 2007, **6**, 183 – 191.

27 Z. Wu, Z. Chen, X. Du, J. M. Logan, J. Sippel, M. Nikolou, K. Kamaras, J. R. Reynolds, D. B. Tanner, A. F. Hebard and A. G. Rinzler, *Science*, 2004, **305**, 1273–1276.

28 J. Hone, M. C. Llaguno, N. M. Nemes, A. T. Johnson, J. E. Fischer, D. A. Walters, M. J. Casavant, J. Schmidt and R. E. Smalley, *Appl. Phys. Lett.*, 2000, **77**, 666–668.

29 *Science of Fullerenes and Carbon Nanotubes*, ed. M. Dresselhaus, G. Dresselhaus and P. Eklund, Academic Press, San Diego, 1996.

30 S. Lisenkov, R. Herchig, S. Patel, R. Vaish, J. Cuozzo and I. Ponomareva, *Nano Lett.*, 2016, **16**, 7008–7012.

31 M. S. Reis and S. Soriano, *Appl. Phys. Lett.*, 2013, **102**, 112903.

32 N. Ma and M. S. Reis, *Sci. Rep.*, 2017, **7**, 13257.

33 Y. Miyazaki, M. Sorai, R. Lin, A. Dworkin, H. Szwarc and J. Godard, *Chem. Phys. Lett.*, 1999, **305**, 293–297.

34 P. A. Heiney, J. E. Fischer, A. R. McGhie, W. J. Romanow, A. M. Denenstein, J. P. McCauley Jr., A. B. Smith and D. E. Cox, *Phys. Rev. Lett.*, 1991, **66**, 2911–2914.

35 R. Tycko, G. Dabbagh, R. M. Fleming, R. C. Haddon, A. V. Makhija and S. M. Zahurak, *Phys. Rev. Lett.*, 1991, **67**, 1886–1889.

36 D. André, A. Dworkin, H. Szwarc, R. Céolin, V. Agafonov, C. Fabre, A. Rassat, L. Straver, P. Bernier and A. Zahab, *Molec. Phys.*, 1992, **76**, 1311–1317.

37 W. I. F. David, R. M. Ibberson, J. C. Matthewman, K. Prassides, T. J. S. Dennis, J. P. Hare, H. W. Kroto, R. Taylor and D. R. M. Walton, *Nature*, 1991, **353**, 147–149.

38 G. V. Tendeloo, S. Amelinckx, S. Muto, M. A. Verheijen, P. H. M. van Loosdrecht and G. Meijer, *Ultramicroscopy*, 1993, **51**, 168 – 188.

39 W. I. F. David, R. M. Ibberson, T. J. S. Dennis, J. P. Hare and K. Prassides, *Europhys. Lett. (EPL)*, 1992, **18**, 219–225.

40 D. L. Dorset and M. P. McCourt, *Acta Cryst. A*, 1994, **50**, 344–351.

41 G. A. Samara, L. V. Hansen, R. A. Assink, B. Morosin, J. E. Schirber and D. Loy, *Phys. Rev. B*, 1993, **47**, 4756–4764.

42 J. E. Fischer, A. R. McGhie, J. K. Estrada, M. Haluška, H. Kuzmany and H.-U. ter Meer, *Phys. Rev. B*, 1996, **53**, 11418–11424.

43 G. Pitsi, J. Caerels and J. Thoen, *Phys. Rev. B*, 1997, **55**, 915–920.

44 G. Kriza, J.-C. Ameline, D. Jérome, A. Dworkin, H. Szwarc, C. Fabre, D. Schütz, A. Rassat, P. Bernier and A. Zahab, *J. Phys. I France*, 1991, **1**, 1361–1364.

45 A. Aznar, P. Lloveras, M. Barrio and J. L. Tamarit, *Eur. Phys. J. Special Topics*, 2017, **226**, 1017–1029.

46 B. Yu, M. Liu, P. W. Egolf and A. Kitanovski, *Int. J. Refrig.*, 2010, **33**, 1029 – 1060.

47 N. P. Kobelev, R. K. Nikolaev, N. S. Sidorov and Y. M. Soifer, *Phys. Sol. State*, 2001, **43**, 2344–2350.

48 A. Planes, T. Castán and A. Saxena, *Phil. Mag.*, 2014, **94**, 1893–1908.

49 M. Álvarez Murga and J. Hodeau, *Carbon*, 2015, **82**, 381 – 407.

50 G. A. Samara, J. E. Schirber, B. Morosin, L. V. Hansen, D. Loy and A. P. Sylwester, *Phys. Rev. Lett.*, 1991, **67**, 3136–3139.

51 C. N. R. Rao, A. Govindaraj, H. N. Aiyer and R. Seshadri, *J. Phys. Chem.*, 1995, **99**, 16814–16816.

52 V. A. Davydov, L. S. Kashevarova, A. V. Rakhmanina, V. M. Senyavin, V. Agafonov, R. Ceolin and H. Szwarc, *J. Exp. Theor. Phys. Lett.*, 1998, **68**, 928–934.

53 E. Stern-Taulats, P. Lloveras, M. Barrio, E. Defay, M. Egilmez, A. Planes, J.-L. Tamarit, L. Mañosa, N. D. Mathur and X. Moya, *APL Mater.*, 2016, **4**, 091102.

54 V. V. Diky, L. S. Zhura, A. G. Kabo, V. Y. Markov and G. J. Kabo, *Fullerene Sci. Techn.*, 2001, **9**, 543–551.

55 An unexpected very large uncertainty of 20% for $(\partial V/\partial T)_p$ at high pressures would result in a relative error in the isothermal entropy changes of 6% and 9% for pressure changes of 0.22 GPa and of 0.59 GPa, respectively.

56 T. Gottschall, E. Stern-Taulats, L. Mañosa, A. Planes, K. P. Skokov and O. Gutfleisch, *Appl. Phys. Lett.*, 2017, **110**, 223904.

57 E. Stern-Taulats, A. Planes, P. Lloveras, M. Barrio, J.-L. Tamarit, S. Pramanick, S. Majumdar, C. Frontera and L. Mañosa, *Phys. Rev. B*, 2014, **89**, 214105.

58 E. Brück, H. Yibole and L. Zhang, *Philos. Trans. A Math. Phys. Eng. Sci.*, 2016, **374**, 20150303.

59 L. Mañosa and A. Planes, *Appl. Phys. Lett.*, 2020, **116**, 050501 and Erratum, **116**, 099901.